Modeling and experimental verification of plasmas induced by high-power nanosecond laser-aluminum interactions in air

B. Wu, Y. C. Shin, H. Pakhal, N. M. Laurendeau, and R. P. Lucht
School of Mechanical Engineering, Purdue University, West Lafayette, Indiana 47907, USA
(Received 5 April 2007; published 31 August 2007)

It has been generally believed in literature that in nanosecond laser ablation, the condensed substrate phase contributes mass to the plasma plume through surface evaporation across the sharp interface between the condensed phase and the vapor or plasma phase. However, this will not be true when laser intensity is sufficiently high. In this case, the target temperature can be greater than the critical temperature, so that the sharp interface between the condensed and gaseous phases disappears and is smeared into a macroscopic transition layer. The substrate should contribute mass to the plasma region mainly through hydrodynamic expansion instead of surface evaporation. Based on this physical mechanism, a numerical model has been developed by solving the one-dimensional hydrodynamic equations over the entire physical domain supplemented by wide-range equations of state. It has been found that model predictions have good agreements with experimental measurement for plasma front location, temperature, and electron number density. This has provided further evidence (at least in the indirect sense), besides the above theoretical analysis, that for nanosecond laser metal ablation in air at sufficiently high intensity, the dominant physical mechanism for mass transfer from the condensed phase to the plasma plume is hydrodynamic expansion instead of surface evaporation. The developed and verified numerical model provides useful means for the investigation of nanosecond laser-induced plasma at high intensities.

DOI: 10.1103/PhysRevE.76.026405 PACS number(s): 52.38.Mf, 52.50.Jm

I. INTRODUCTION

Nanosecond pulsed-laser ablation of materials has been investigated for many years because of applications in material removal from solid parts or thin-film deposition [1]. Understanding the fundamental aspects of pulsed laser-matter interactions has also generated considerable interest in the research community. The irradiation of a target with a laser pulse having sufficiently high intensity produces a high-temperature plasma. The laser-induced plasma becomes an important part of the laser ablation process. Therefore, to understand laser-matter interactions, investigating the dynamics of the plasma plume is essential.

During nanosecond-pulsed laser ablation, if the target surface temperature does not closely approach or exceed the thermodynamic critical temperature (that is, when the laser fluence is below a certain threshold), the process is characterized by the formation of a sharp liquid-vapor interface [2]. All vapor molecules leaving the liquid-vapor interface during laser evaporation have velocity components in the direction away from the surface at the interface and develop an equilibrium velocity distribution within several mean free paths. The thin region adjacent to the interface, where the normal velocity of vapor molecules transforms from a nonequilibrium to an equilibrium distribution is called the Knudsen Layer (KL) [2]. The vapor flow above KL can be considered to be a gas dynamic flow satisfying the continuum approximation. In the numerical modeling of laser evaporation, KL is treated as a discontinuity and provides boundary conditions that couple the heat transfer equation for the target with gas dynamic equations for the vapor and ambient gas phase [2–6].

When the laser intensity is sufficiently high, the surface evaporation process as discussed above should not be the dominant physical mechanism for mass transfer from the condensed phase to the gaseous phase. In this case, the target temperature can be greater than the critical temperature, so that the sharp interface between the condensed and gaseous phases disappears and is smeared into a macroscopic transition layer [7]. Under such conditions, the condensed phase should contribute mass to the plasma region mainly through hydrodynamic expansion, and the laser ablation process should be described by solving the hydrodynamic equations for the whole physical domain, supplemented with wide-range equations of state [7]. The experimental investigation of laser ablation of aluminum in Ref. [8] indicates that the aluminum target surface temperature is already close to and may be even higher than the critical temperature when the laser irradiance approaches 0.5 GW/cm^2 for laser-pulse duration in the order of around 10 ns. Therefore, for nanosecond pulses with irradiances of several GW/cm^2, the plasma induced by laser ablation of aluminum should be described through the hydrodynamic equations for the whole physical domain, where the condensed phase contributes mass to the plasma region through hydrodynamic expansion. Unfortunately, the physical mechanism discussed above, although it seems to be true based on theoretical analysis, has rarely been rigorously verified through experimental and numerical work in literature for common metals such as aluminum. This paper provides a confirmation of such a mechanism through both modeling and experiments.

In this paper, a numerical model is developed for the plasma induced by the interaction of high-power nanosecond laser pulses with aluminum in air. The one-dimensional (1D) hydrodynamic equations are solved numerically for the whole involved physical domain supplemented by wide-range equations of state (EOS).

Experimental measurements are also performed on the laser-induced plasma. Although much previous experimental

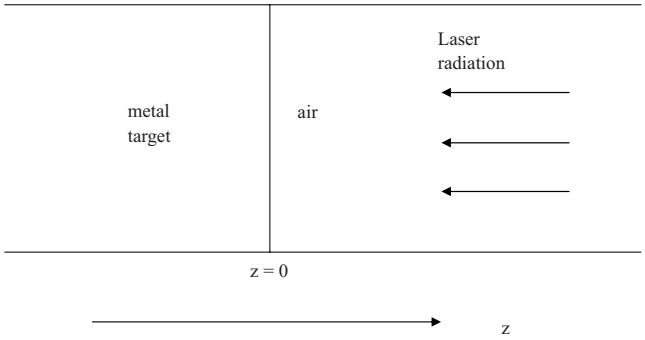

FIG. 1. Schematic diagram of the model setup.

work has been carried out for laser-induced plasmas [9–15], experimental measurements of plasma parameters at its early stage ($t \leq 50$ ns) are quite scarce. In this paper, the plasma transient front location, plasma electronic temperature, and electron number density are determined in the early stage through high-speed photography and emission spectroscopy.

Finally, the experimental measurements are compared with the simulations to verify the developed model and also to test the validity of the fundamental physical mechanism assumed by the model for mass transfer from the condensed phase to plasma region in high-intensity nanosecond laser aluminum interaction in air. This approach of an indirect testing of the mass transfer physical mechanism is taken because a direct experimental observation, although quite ideal, is very difficult. Another contribution of this work is that the developed and verified numerical model can become a useful tool for the investigation of high-intensity nanosecond laser-induced plasma, laser ablation, and many other relevant applications.

II. MODELING APPROACH

Figure 1 is a schematic diagram of the model for the interaction of laser radiation with a target surface. Initially, the metal surface is located at $z=0$, the metal target is at $z<0$, and the air is at $z>0$. Laser radiation comes in the $-z$ direction. For this system, the one-dimensional hydrodynamic equations, governing conservation of mass, momentum, and energy, can be expressed as Refs. [16,17]

$$\frac{\partial U}{\partial t} + \frac{\partial F_z}{\partial z} = \frac{\partial S_z}{\partial z}, \tag{1}$$

where

$$U = \begin{bmatrix} \rho_1 \\ \rho_2 \\ \rho u \\ E + \frac{1}{2}\rho u^2 \end{bmatrix},$$

$$F_z = \begin{bmatrix} \rho_1 u \\ \rho_2 u \\ \rho u^2 + P \\ u\left(E + \frac{1}{2}\rho u^2 + P\right) \end{bmatrix},$$

$$S_z = \begin{bmatrix} 0 \\ 0 \\ 0 \\ -q + k\frac{\partial T}{\partial z} + I \end{bmatrix}.$$

The total density is defined as $\rho=\rho_1+\rho_2$, where ρ_1 and ρ_2 are the densities of metal and air, respectively. Furthermore, u is the velocity, P is the pressure, E is the volumetric internal energy, T is the temperature, k is the thermal conductivity, I is the net flux in laser radiation in $-z$ direction, and q is the radiative heat flux in the z direction. The latter can be obtained by solving the radiative transfer equation in the diffusion approximation [17] as follows:

$$\frac{\partial}{\partial z}(q_v) + ck_v U_v = ck_v U_{bv},$$

$$q_v = -\frac{c}{3k_v}\frac{\partial U_v}{\partial z},$$

$$U_{bv} = \frac{8\pi h v^3}{c^3[\exp(hv/kT) - 1]},$$

$$q = \int_v q_v dv, \tag{2}$$

where U_v and U_{bv} are the spectral energy density for radiation and blackbody radiation, respectively, c is the speed of light, and k_v is the absorption coefficient, where the subscript v denotes the radiative frequency. Equation (2) can be solved using a multigroup approximation [17].

The hydrodynamic equations must be supplemented by wide-range equations of state (EOS). As mentioned earlier, for an aluminum target irradiated by an intense nanosecond laser pulse, the sharp interface between the condensed and gaseous phases disappears and is smeared into a macroscopic transition layer. Hence, the hydrodynamic equations must be solved for the entire physical domain, including the transition layer across which the density changes very rapidly, the high-density condensed phase below the transition layer, and the low-density and high-temperature plasma above the transition layer. Therefore, an equation of state is needed that can cover a very wide range of temperature and density. In this work, the quotidian equation of state (QEOS) [18], which satisfies well the above requirement for an aluminum target, is adopted.

The QEOS is a wide-range equation of state model, which is very attractive for numerical hydrodynamic simulations owing to its semianalytical structure [18]. It can produce

quantities such as energy, pressure, ionization state, and entropy as smooth functions of temperature and density, and this will remarkably reduce numerical noise, which is very important for a numerical hydrodynamic code. In QEOS, the electronic properties are obtained from a modified Thomas-Fermi statistical model, while the ion thermal motion is described by the Cowan model [18]. The input for the QEOS model includes the material atomic number, bulk modulus, and normal solid density, based on which an EOS table can be generated, which lists material energy, pressure, and other states as functions of temperature T and density ρ. The applicability of the QEOS model to aluminum has been demonstrated in Ref. [18], and it should have reasonably good overall accuracy for the entire temperature and density domain involved in the hydrodynamic simulation in this work. It has also been applied by many researchers in literature for hydrodynamic simulations of laser-matter interactions involving a wide range of temperatures and densities [19].

For the QEOS model, thermodynamic functions, such as pressure and energy, are obtained from the Helmholtz free energy, which is given via the additive assumption by

$$F = F_i + F_e + F_b, \tag{3}$$

where F_i, F_e, and F_b are the ion free energy, the semiclassical selectron free energy, and the semiempirical correction for chemical bonding effects in the solid state, respectively.

Based on the free energy, the pressure p, the entropy S, and the energy E are obtained according to the following equations:

$$p_i = \rho^2 \frac{\partial F_i}{\partial \rho}, \quad S_i = -\frac{\partial F_i}{\partial T_i}, \quad E_i = F_i + T_i S_i, \tag{4}$$

$$p_b = \rho^2 \frac{\partial F_b}{\partial \rho}, \quad S_b = -\frac{\partial F_b}{\partial T_e}, \quad E_b = F_b + T_e S_b, \tag{5}$$

$$p_e = \rho^2 \frac{\partial F_e}{\partial \rho}, \quad S_e = -\frac{\partial F_e}{\partial T_e}, \quad E_e = F_e + T_e S_e. \tag{6}$$

The total pressure p and energy E are then given by

$$p = p_e + p_i + p_b, \quad E = E_e + E_i + E_b. \tag{7}$$

For the ion portion, the Cowan model is applied [18], which can be divided into two parts, a "structural part" and a "phenomenological part." The structural model constructs thermodynamic functions in terms of a known melting temperature $T_m(\rho)$ and Debye temperature $\Theta_D(\rho)$. Two scaling variables, u and w, are defined by

$$u = \Theta_D(\rho)/T, \quad w = T_m(\rho)/T. \tag{8}$$

The ion free energy is thus given by

$$F_i = (k_b T/m) f(u,w), \tag{9}$$

where m is the mass per atom. For $f(u,w)$, different expressions are applied for low-temperature solid $(w>1, u>3)$,

$$f = \frac{9u}{8} + 3\ln[1-\exp(-u)] - \frac{\pi^4}{5u^3} + \exp(-u)\left[3 + \frac{9}{u} + \frac{18}{u^2} + \frac{18}{u^3}\right], \tag{10}$$

for a high-temperature solid $(w>1, u<3)$,

$$f = -1 + 3\ln u + (3u^2/40 - u^4/2240), \tag{11}$$

and for the fluid phase $(w<1)$,

$$f = -\frac{11}{2} + \frac{9}{2} w^{1/3} + \frac{3}{2}\ln\left(\frac{u^2}{w}\right). \tag{12}$$

The "phenomenological part" of the Cowan model attempts to predict the melting temperature T_m and the Debye temperature Θ_D via

$$k_b T_m = 0.32[\xi^{2b+10/3}/(1+\xi)^4] \quad (\text{eV}), \tag{13}$$

$$k_b \Theta_D = [1.68/(Z+22)][\xi^{b+2}/(1+\xi)^2] \quad (\text{eV}), \tag{14}$$

$$\gamma_s = b + 2/(1+\xi), \tag{15}$$

where $b=0.6Z^{1/9}$, $\xi=\rho/\rho_{ref}$, and Z is the atomic number. The reference density is given by

$$\rho_{ref} = (A/9Z^{0.3}) \quad (\text{g/cm}^3), \tag{16}$$

where A is the atomic weight.

The electronic properties are obtained from a modified Thomas-Fermi statistical model. In Thomas-Fermi theory, the electrons are treated as a charged fluid surrounding the nucleus and the properties of this electron gas are obtained from finite-temperature Fermi-Dirac statistics. Each nucleus is located at the center of a spherical cavity of radius $R_0 = (3/4\pi n_i)^{1/3}$, where n_i is the total ion number density. The cavity contains sufficient electrons to be electrically neutral and other ions are assumed to remain outside the sphere. By solving the Poisson equation coupled with the formula for a finite-temperature semiclassical electron gas, the electrostatic potential, etc., within the ion sphere can be obtained, and then F_e (and thus p_e and E_e) can be calculated.

Thomas-Fermi theory gives a positive pressure induced by a free electron gas, which will be a few megabars at zero temperature for metallic electron densities. In reality for cold matter near the normal solid density, the chemical bonds support a certain finite matter density at zero total pressure. In the QEOS model, this effect is taken into account by adding the semiempirical bonding correction F_b.

Similar to Ref. [19], transport properties, such as the thermal and electrical conductivities, are obtained using the model proposed by Lee and More [20,21], where the transport coefficients are calculated using the stationary Boltzmann equation in the relaxation time approximation. In the current work, the Boltzmann equation for the electron distribution function is solved and then the solution is applied to calculate the flux of electrical current and energy, from which the transport coefficients can be obtained. Based on the dc electrical conductivity, the material absorption coefficient due to free electrons and the complex index of refrac-

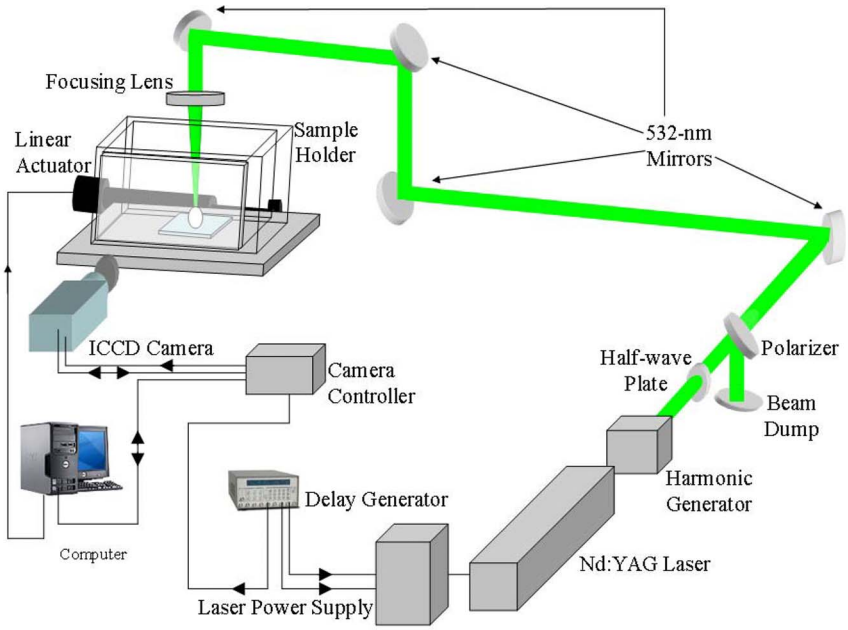

FIG. 2. (Color online) Experimental system for high-speed photography.

tion can be determined using Drude theory [19,22,23].

The ionization of air can be calculated by solving relevant Saha equations [24]. Once the electron number density n_e is obtained, the air pressure can be calculated as [17]

$$P = k_b T(n_p + n_e), \tag{17}$$

where k_b is the Boltzmann constant and n_p is the total number density of heavy particles, including both neutral particles and ions. If ionization of air does not occur, Eq. (17) becomes the ideal gas equation of state, $P=k_b T n_p$. Once air is ionized, laser energy can be absorbed through inverse bremsstrahlung and photoionization effects [25], which has been considered in the model.

The hydrodynamic equations are solved using a finite difference scheme [26–28]. The procedure in Ref. [28] is an essentially nonoscillatory scheme that does not require field-by-field decomposition or staggered grids. It is robust, fast, and relatively easy to implement. The numerical flux is constructed based on certain limiters, with updating of the solution vector U using TVD Runge-Kutta time discretizations. The numerical domain size was chosen such that interfaces between disturbed and undisturbed material do not reach the domain boundaries. In all cases, the convergence of the scheme was checked by further reducing the grid size, if significant changes occurred in the simulation, a finer grid was implemented.

III. EXPERIMENTAL APPARATUS AND TECHNIQUES

The laser used for all experiments is a Continuum Surelite III Nd:YAG laser. Employing a second harmonic generator, the laser can emit a 6-ns-full-width-half-maximum (FWHM) pulse at 532 nm, with pulse energy up to around 800 mJ.

Figure 2 is a three-dimensional view of the experimental

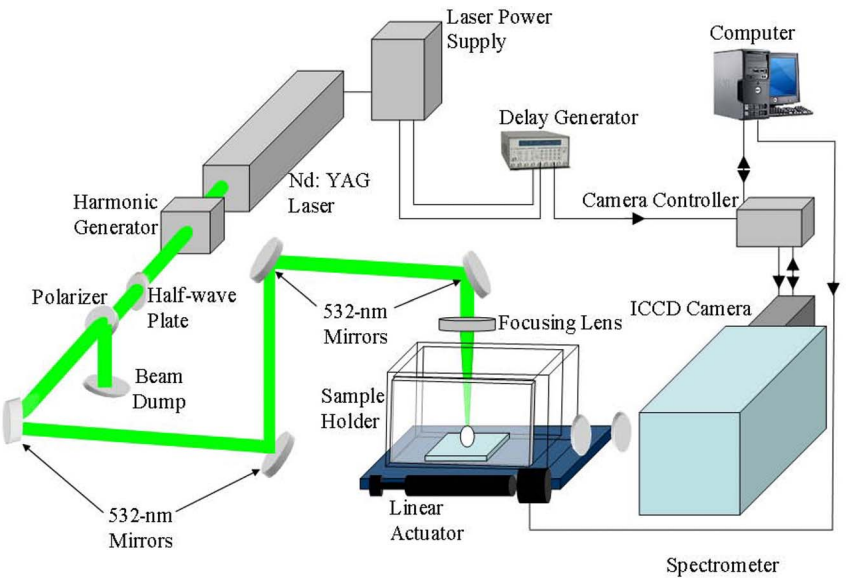

FIG. 3. (Color online) Experimental system for emission spectroscopy.

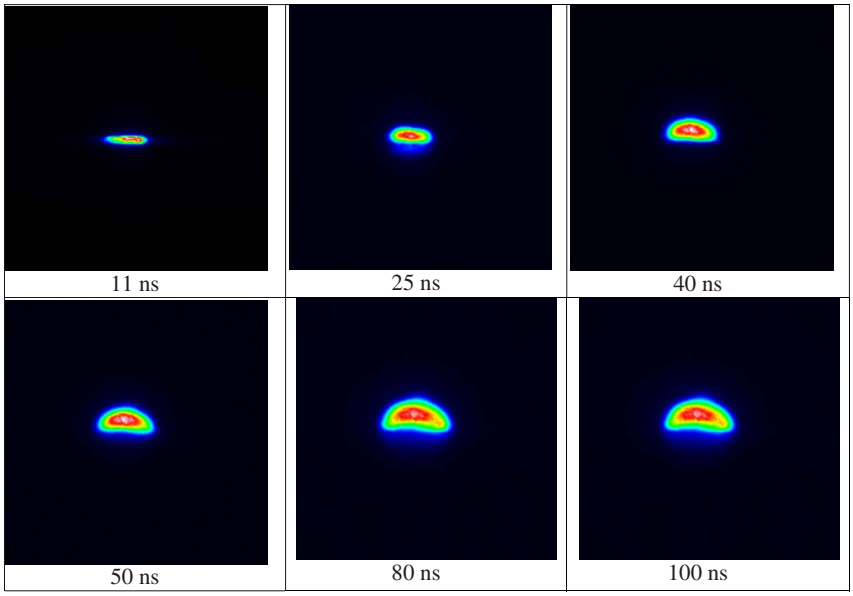

FIG. 4. (Color online) Images of plasma plume produced during laser ablation of aluminum in air at 8.1 GW/cm^2.

system for high-speed photography. An ICCD camera (Princeton Instruments PI-MAX) was used to collect all images of plasma formation. A zero-order half-wave plate mounted on a rotary stage and a thin-film polarizer were used to control laser power. A group of 532 nm mirrors was employed to direct the laser beam to the focusing lens, as shown in Fig. 2.

A 100 mm focusing lens was used to deliver the laser beam onto the sample, while the PI-MAX ICCD camera was used to capture images of the plasma plume as a function of time. The camera had a gate width of 2 ns for the first 100 ns and a gate width of 5 ns for later delay times. The laser spot size on the sample surface was around 0.45 mm. For each delay time, ten images were captured by the ICCD camera. Plasma plume heights were extracted from each image, with average values determined at each delay time.

The experimental system for emission spectroscopy is quite similar to that for high-speed photography. The laser ablation part of the system remains the same. The diagnostic system is changed, with collection optics and a spectrometer being added to the system. Figure 3 is a three-dimensional view of the emission spectroscopy system. The emission radiated from the plasma was collected at a 90° angle by the collection optics and focused onto the entrance slit of the spectrometer. Two biconvex lenses were used with focal lengths of 100 and 200 mm, respectively. The ICCD camera was operated in its spectroscopy mode, with a gate width of 2 ns for the first 100 ns and at a gate width of 5 ns thereafter. Ten spectra were obtained for each delay time. The spectra were then averaged over ten acquisitions to improve the signal-to-noise ratio. Background noise was automatically subtracted from the acquired spectra. Since a continuum is observed at initial delay times owing to the nature of the plasma, it was not possible to differentiate between the continuum and noise. Therefore, quantitative spectra could only be obtained at a much later delay, when the continuum had decayed to zero. The noise was almost absent in these cases, ensuring a very high signal-to-noise ratio.

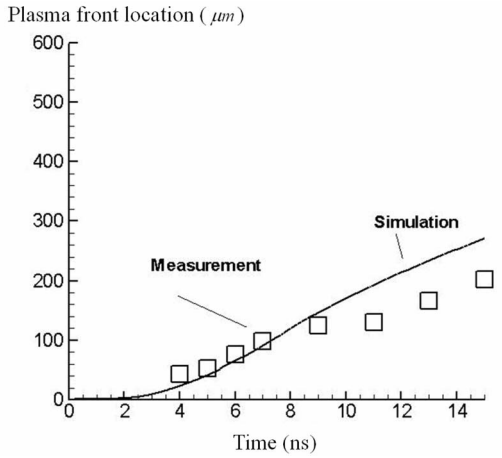

FIG. 5. Transient front location for plasma induced by laser ablation of aluminum in air at 5 GW/cm^2.

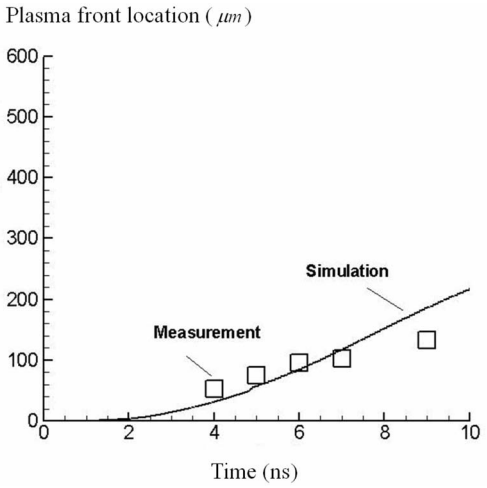

FIG. 6. Transient front location for plasma induced by laser ablation of aluminum in air at 8.1 GW/cm^2.

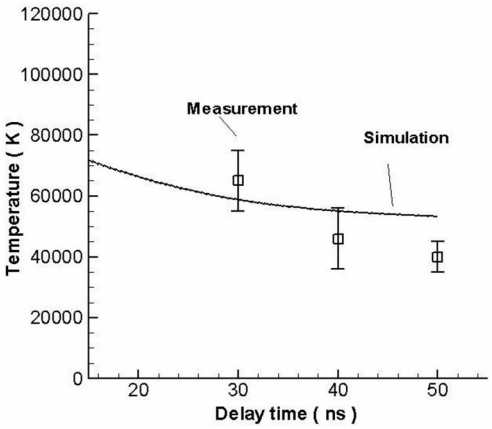

FIG. 7. Transient temperature of plasma induced by laser ablation of aluminum in air at 3.8 GW/cm^2.

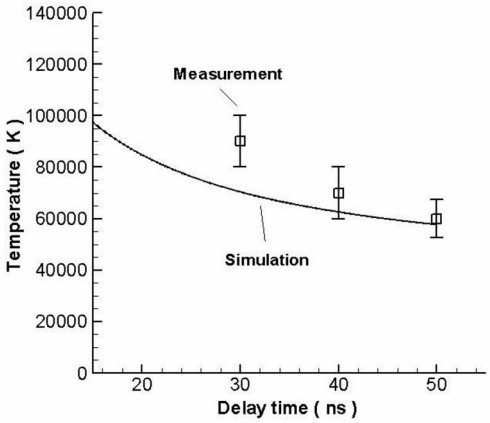

FIG. 8. Transient electron temperature for plasma induced by laser ablation of aluminum in air at 8 GW/cm^2.

For the laser irradiances used in this study, the spectrum of the laser-induced plasma in its early stages is dominated by continuum emission; moreover, the emission lines are significantly broadened by Stark broadening owing to high electron number densities. The lines are also shifted due to the Stark effect. Because of the high FWHM of these lines, overlap is significant. Line overlap not only complicates the appearance of the spectrum, but also blends into the continuum. This feature has been referred to as a "pseudocontinuum" in the literature. The presence of a pseudocontinuum does not allow us to subtract the continuum from the spectrum, since relative intensities are not known.

To add further to the complications of the observed spectra, the plasma is optically thick owing to its relatively large spot size. This leads to radiation trapping and the appearance of self-reversed structures in the emission spectrum. Since radiation is trapped by relatively cooler and less dense parts of the plasma at the periphery, the Stark shift is almost zero. Therefore, the self-reversed structures do not shift and a different line profile needs to be calculated to account for this effect. All of these factors make it impossible to calculate temperature and electron number density directly from the measured spectrum. Instead, a plasma emission model was developed based on the radiative transfer equation. The model inputs are the plasma temperature and electron number density; the output is the plasma spectrum. The input of the model is varied until the output matches the measured spectrum. In this way, the plasma temperature and electron number density can be determined, as discussed in detail in a separate paper [29].

IV. COMPARISON BETWEEN SIMULATED AND EXPERIMENTAL RESULTS

The plasma images taken by the ICCD camera are shown in Fig. 4, which indicate that plasma lateral expansion is not significant for the first 50 ns, and thus it is reasonable to apply a 1D hydrodynamic model to simulate plasma evolution during this time. The 1D hydrodynamic model provides the spatial distributions of temperature, density, and velocity over the entire physical domain, from which the high-temperature, low-density plasma region can be easily identified, where the matter is moving rapidly in the $+z$ direction.

Figure 5 shows the transient plasma-front location at an irradiance of 5 GW/cm^2. The experimental measurements obtained via high-speed photography are close to the simulation results based on the hydrodynamic model. The plasma front starts propagating at around $t=2$ ns, and reaches a height of around 200 μm at $t=15$ ns. The average front propagation velocity is around 15 000 m/s during this period. The transient plasma-front location is not significantly different at an irradiance of 8.1 GW/cm^2, which is shown in Fig. 6. The agreement between simulations and experimental measurements is still reasonably good.

The plasma emission spectrum can be measured using the setup shown in Fig. 3, from which the plasma electron number density and electron temperature can be obtained via a plasma emission model [29]. To the authors' best knowledge, early-stage comparisons between simulations and experiments for electron temperature and electron number density have been rarely reported in literature for plasmas induced by high-power ($\sim$GW/cm^2), nanosecond laser ablation of common metals (such as aluminum) in air.

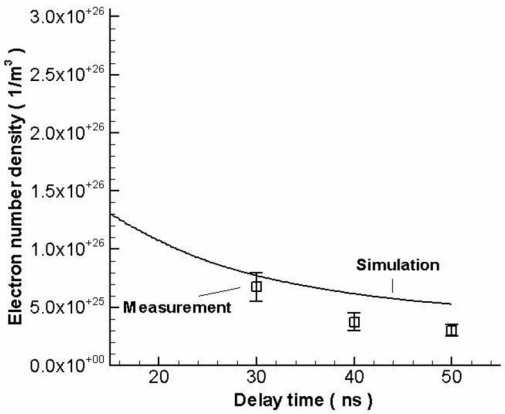

FIG. 9. Transient electron number density for plasma induced by laser ablation of aluminum in air at 3.8 GW/cm^2.

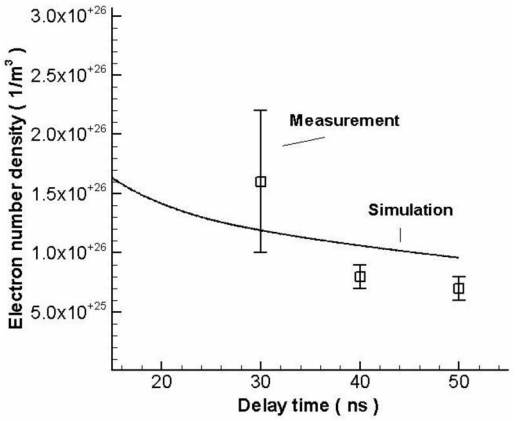

FIG. 10. Transient electron number density for plasma induced by laser ablation of aluminum in air at 8 GW/cm^2.

Figures 7 and 8 show the transient temperature of the plasma at irradiances of 3.8 and 8.0 GW/cm^2, respectively. The agreement between simulation and measurements is quite good. At 3.8 GW/cm^2, the plasma temperature decreases from around 65 000 K at 30 ns to around 40 000 K at 50 ns, while at 8.0 GW/cm^2, the temperature decreases from around 90 000 K at 30 ns to around 60 000 K at 50 ns. As expected, the electron temperature is greater at higher laser irradiances. It can also be seen from Figs. 7 and 8 that the plasma cooling rate decreases somewhat with increasing time after laser ablation.

Figures 9 and 10 show the transient electron number density of the plasma at irradiances of 3.8 and 8.0 GW/cm^2, respectively. The simulations still adequately represent the experimental measurements. At 3.8 GW/cm^2, the plasma electron number density decreases from around 7.0×10^{25} m^{-3} at 30 ns to around 3.0×10^{25} m^{-3} at 50 ns, while at 8.0 GW/cm^2, the electron number density decreases from around 16.0×10^{25} m^{-3} at 30 ns to around 7.0×10^{25} m^{-3} at 50 ns. As expected, the electron number density is also greater at higher laser irradiances. Similar to the plasma cooling rate, Figs. 9 and 10 show that the rate of reduction in plasma electron number density decreases with increasing time after laser ablation.

In this paper, it has been assumed that the electron temperature is equal to ion temperature. This assumption can generally be verified by considering the relaxation time τ_{ei} of energy exchange between electrons and the ions [17], which has been found to be generally around ~0.1 ns or less in the simulations. This is much smaller than the laser pulse duration. Therefore assuming the same temperature for the electrons and ions should be reasonable.

It has been found in the calculations that in the plasma region the spectral radiation energy density U_v is generally not equal to the blackbody radiation energy density U_{bv} at the same temperature and frequency, and in this sense the plasma radiation is generally not a blackbody radiation. This is demonstrated in Fig. 11, which shows the ratio of plasma

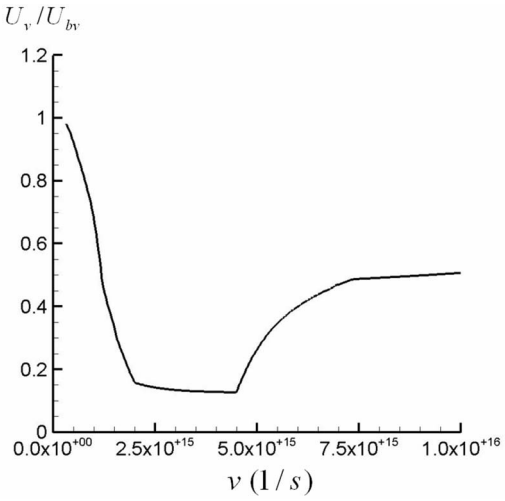

FIG. 11. The ratio of plasma spectral radiation energy density over blackbody radiation energy density U_v/U_{bv} as a function of frequency υ at $t=8$ ns and $z=40$ μm (laser power density: 8.1 GW/cm^2).

spectral radiation energy density over blackbody radiation energy density U_v/U_{bv} as a function of frequency υ at $t=8$ ns and $z=40$ μm (laser power density: 8.1 GW/cm^2).

V. CONCLUSIONS

The plasma induced by a high-power, nanosecond laser-metal interaction in air has been investigated through both numerical modeling and experimental measurements. Because of the high laser irradiance, the sharp interface between the condensed and gaseous phases disappears and is smeared into a macroscopic transition layer. Hence, the early-stage evolution of the plasma was simulated by solving the hydrodynamic equations over the entire physical domain, supplemented with a wide-ranging equation of state. Good agreement between simulations and experiments has verified the developed 1D model, and has provided important evidence that for nanosecond laser-metal ablation in air at sufficiently high intensity, the dominant physical mechanism for mass transfer from the condensed phase to the plasma plume is hydrodynamic expansion instead of surface evaporation. For the laser irradiances of this study, the plasma temperature is around 40 000–90 000 K, and the plasma electron number density is around 3.0×10^{25} m^{-3} to 16.0×10^{25} m^{-3} at delay times of around 30–50 ns. Certainly, because the involved process is very complicated, further work is still required to have a final conclusion on this issue.

ACKNOWLEDGMENTS

The authors would like to thank Dr. D. A. Young for discussions on QEOS. The authors wish to gratefully acknowledge the financial support provided by the National Science Foundation (Grant No. IIP0538786) and the State of Indiana 21st Century R&T Fund.

[1] B. Braren, J. J. Dubowski, and D. P. Norton, *Laser Ablation in Materials Processing: Fundamentals and Applications* (Material Research Society, Pittsburgh, 1993).
[2] S. H. Jeong, R. Greif, and R. E. Russo, *Proceedings of ASME Heat Transfer Division, Vol. 1* (ASME, New York, 1997), pp. 63–73.
[3] S. I. Anisimov, Sov. Phys. JETP **27**, 182 (1968).
[4] C. J. Knight, AIAA J. **17**, 519 (1979).
[5] C. J. Knight, AIAA J. **20**, 950 (1982).
[6] B. Wu and Y. C. Shin, J. Appl. Phys. **99**, 084310 (2006).
[7] S. I. Anisimov, V. A. Gal'burt, M. F. Ivanov, I. E. Poyurovskaya, and V. I. Fisher, Sov. Phys. Tech. Phys. **24**, 295 (1979).
[8] J. M. Fishburn, M. J. Withford, D. W. Coutts, and J. A. Piper, Appl. Surf. Sci. **252**, 5182 (2006).
[9] X. Zeng, X. Mao, S. S. Mao, J. H. Yoo, R. Greif, and R. E. Russoa, J. Appl. Phys. **95**, 816 (2004).
[10] M. Sabsabi and P. Cielo, Appl. Spectrosc. **49**, 499 (1995).
[11] L. A. Doyle, G. W. Martin, A. Al-Khateeb, I. Weaver, D. Riley, M. J. Lamb, T. Morrow, and C. L. S. Lewis, Appl. Surf. Sci. **127**, 716 (1998).
[12] H. Wang, A. P. Salzberg, and B. R. Weiner, Appl. Phys. Lett. **59**, 935 (1991).
[13] B. Y. Man, Appl. Phys. B: Lasers Opt. **67**, 241 (1998).
[14] B. Y. Man, X. T. Wang, and A. H. Liu, J. Appl. Phys. **83**, 3509 (1998).
[15] J. Hermann, A. L. Thomann, C. Boulmer-Leborgne, B. Dubreuil, M. L. DeGiorgi, A. Perrone, A. Luches, and I. N. Mihailescu, J. Appl. Phys. **77**, 2928 (1995).
[16] A. V. Gusarov and I. Smurov, J. Appl. Phys. **97**, 014307 (2005).
[17] Y. B. Zel'dovich and Y. P. Raizer, *Physics of Shock Waves and High-Temperature Hydrodynamic Phenomena* (Academic Press, New York and London, 1966).
[18] R. M. More, K. H. Warren, D. A. Young, and G. B. Zimmerman, Phys. Fluids **31**, 3059 (1988).
[19] F. Vidal, T. W. Johnston, S. Laville, O. Barthelemy, M. Chaker, B. Le Drogoff, J. Margot, and M. Sabsabi, Phys. Rev. Lett. **86**, 2573 (2001).
[20] Y. T. Lee and R. M. More, Phys. Fluids **27**, 1273 (1984).
[21] M. P. Desjarlais, Contrib. Plasma Phys. **41**, 267 (2001).
[22] F. L. Pedrotti and L. S. Pedrotti, *Introduction to Optics* (Prentice Hall, Englewood Cliffs, NJ, 1993).
[23] V. L. Ginzburg, *Propagation of Electromagnetic Waves in Plasma* (Gordon and Breach, Science Publishers, Inc., New York, 1961).
[24] M. R. Zaghloul, M. A. Bourham, and J. M. Doster, J. Phys. D **33**, 977 (2000).
[25] Y. V. Boyko, N. P. Kozlov, Y. M. Grishin, Y. S. Protasov, A. S. Kamrukov, and S. N. Chuvashev, *Thermodynamic and Optical Properties of Ionized Gases at Temperatures up to 100 Ev* (Hemisphere Publishing Corporation, New York, 1991).
[26] R. J. LeVeque, *Numerical Methods for Conservation Laws* (Birkhäuser, Basel, Boston, Berlin, 1992).
[27] J. C. Tannehill, D. A. Anderson, and R. H. Pletcher, *Computational Fluid Mechanics and Heat Transfer*, 2nd ed. (Taylor and Francis, London, 1997).
[28] X. D. Liu and S. Osher, J. Comput. Phys. **142**, 304 (1998).
[29] H. R. Pakhal, R. P. Lucht, and N. M. Laurendeau, Appl. Phys. B: Lasers Opt. (to be published).